ISSN 0253-9837
CN 21-1601/O6

催化学报 Chinese Journal of Catalysis

www.cjcatal.org

Volume 40 | Number 1 | January 2019

Science Press

Editors-in-Chief Can Li (李灿) Tao Zhang (张涛)
Transaction of The Catalysis Society of China

催化学报 CHINESE JOURNAL OF CATALYSIS January 2019 Vol. 40 No. 1 pages 1–000

科学出版社

2019
Vol. 40 No. 1

Chinese Journal of Catalysis

2019年
第40卷 第1期

In This Issue

Cover: Xi's group controls the synthesis of the silk-like FeS_2/NiS_2 hybrid nanocrystal. The material has rich interfaces and defects, which is beneficial to enhance its catalytic performance. The picture shows the flexible battery assembled by this catalyst and their promising application. Read more about the article behind the cover on pages 43–51.

封面: 席聘贤课题组控制合成了丝绸状纳米结构(FeS_2/NiS_2). 该材料具有丰富的界面和缺陷, 有利于提升其催化性能. 见本期第 43–51 页.

About the Journal

Chinese Journal of Catalysis is an international journal published monthly by Chinese Chemical Society, Dalian Institute of Chemical Physics, Chinese Academy of Sciences, and Elsevier. The journal publishes original, rigorous, and scholarly contributions in the fields of heterogeneous and homogeneous catalysis in English or in both English and Chinese. The scope of the journal includes:

- New trends in catalysis for applications in energy production, environmental protection, and production of new materials, petroleum chemicals, and fine chemicals;
- Scientific foundation for the preparation and activation of catalysts of commercial interest or their representative models;
- Spectroscopic methods for structural characterization, especially methods for in situ characterization;
- New theoretical methods of potential practical interest and impact in the science and applications of catalysis and catalytic reaction;
- Relationship between homogeneous and heterogeneous catalysis;
- Theoretical studies on the structure and reactivity of catalysts.
- The journal also accepts contributions dealing with photo-catalysis, bio-catalysis, and surface science and chemical kinetics issues related to catalysis.

Types of Contributions

- ***Reviews*** deal with topics of current interest in the areas covered by this journal. Reviews are surveys, with entire, systematic, and important information, of recent progress in important topics of catalysis. Rather than an assemblage of detailed information or a complete literature survey, a critically selected treatment of the material is desired. Unsolved problems and possible developments should also be discussed. Authors should have published articles in the field. Reviews should have more than 80 references.
- ***Communications*** rapidly report studies with significant innovation and major academic value. They are limited to four Journal pages. After publication, their full-text papers can also be submitted to this or other journals.
- ***Articles*** are original full-text reports on innovative, systematic and completed research on catalysis.
- ***Highlights*** describe and comment on very important new results in the original research of a third person with a view to highlight their significance. The results should be presented clearly and concisely without the comprehensive details required for an original article.
- ***Perspectives*** are short reviews of recent developments in an established or developing topical field. The authors should offer a critical assessment of the trend of the field, rather than a summary of literatures.
- ***Viewpoints*** describe the results of original research in general in some area, with a view to highlighting the progress, analyzing the major problems, and commenting the possible research target and direction in the future.

Impact Factor

2017 SCI Impact Factor: **3.525**
2017 SCI 5-Year Impact Factor: 2.736

Abstracting and Indexing

Abstract Journals (VINITI)
Cambridge Scientific Abstracts (CIG)
Catalysts & Catalysed Reactions (RSC)
Current Contents/Engineering, Computing and Technology (Clarivate Analytics ISI)
Chemical Abstract Service/SciFinder (CAS)
Chemistry Citation Index (Clarivate Analytics ISI)
Japan Information Center of Science and Technology
Journal Citation Reports/Science Edition (Clarivate Analytics ISI)
Science Citation Index Expanded (Clarivate Analytics ISI)
SCOPUS (Elsevier)
Web of Science (Clarivate Analytics ISI)

Chinese Journal of Catalysis

2019
Vol. 40 No. 1

Publication Monthly (12 issues)
Started in March 1980
Transaction of The Catalysis Society of China
Superintended by
Chinese Academy of Sciences (CAS)
Sponsored by
Chinese Chemical Society and Dalian Institute of Chemical Physics, CAS
Editors-in-Chief Can Li, Tao Zhang
Edited by Editorial Board of
Chinese Journal of Catalysis
Tel.: +86-411-84379240
E-mail: cjcatal@dicp.ac.cn
Add.: Dalian Institute of Chemical Physics, CAS, 457 Zhongshan Road, Dalian 116023, Liaoning, China
Published by Science Press
Distributed by Science Press,
16 Donghuangchenggen North Street, Beijing 100717, China, Tel: +86-10-64017032
E-mail: sales_journal@mail.sciencep.com
Subscription Agents
Domestic All Local Post Offices in China
Foreign China International Book Trading Corporation, P.O.Box 399, Beijing 100044, China
Printed by
Dalian Haida Printing Company, Limited
Price $60

月刊 SCI收录 1980年3月创刊
中国化学会催化学会会刊
主管 中国科学院
主办 中国化学会
中国科学院大连化学物理研究所
主编 李 灿 张 涛
编辑 《催化学报》编辑委员会
出版 科学出版社
编辑部联系方式:
地址: 大连市沙河口区中山路 457 号
中国科学院大连化学物理研究所
邮编: 116023
电话: (0411)84379240
传真: (0411)84379543
电子信箱: cjcatal@dicp.ac.cn

国内统一连续出版物号 CN 21-1601/O6
国际标准连续出版物号 ISSN 0253-9837
CODEN THHPD3
广告经营许可证号 2013003
总发行 科学出版社
北京东黄城根北街16号, 邮编: 100717
电话: (010) 64017032
E-mail: sales_journal@mail.sciencep.com
国内订购 全国各地邮政局
邮发代号 8-93
国外订购 中国国际图书贸易总公司
北京399信箱 邮编 100044
国外发行代号 M417
印刷 大连海大印刷有限公司
定价 60元

公 开 发 行

The Fifth Editorial Board of *Chinese Journal of Catalysis*
《催化学报》第五届编辑委员会

Online Submission https://mc03.manuscriptcentral.com/cjcatal, http://www.elsevier.com/locate/chnjc
Homepage http://www.cjcatal.org, http://www.journals.elsevier.com/chinese-journal-of-catalysis

available at www.sciencedirect.com

ScienceDirect

journal homepage: www.elsevier.com/locate/chnjc

Chinese Journal of Catalysis

Graphical Contents

Academic discussion

Chin. J. Catal., 2019, 40: 1–3 doi: 10.1016/S1872-2067(18)63188-2

Comment On the correction of gas-phase signals during IR operando analyses

Frederic Meunier *
Institut de Recherches sur la Catalyse et l'Environnement, France

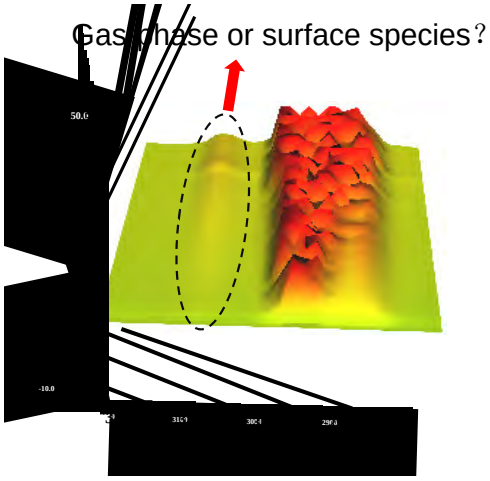

The accuracy of dual beam Fourier transform infrared (DB-FTIR) spectrometer in eliminating the interference of gas-phase molecular vibration in gas/solid heterogeneous catalysis under reaction conditions is discussed.

Reviews

Chin. J. Catal., 2019, 40: 4–22 doi: 10.1016/S1872-2067(18)63177-8

Recent advances in one-dimensional nanostructures for energy electrocatalysis

Ping Li, Wei Chen *
Changchun Institution of Applied Chemistry, Chinese Academic of Science; University of Science and Technology of China

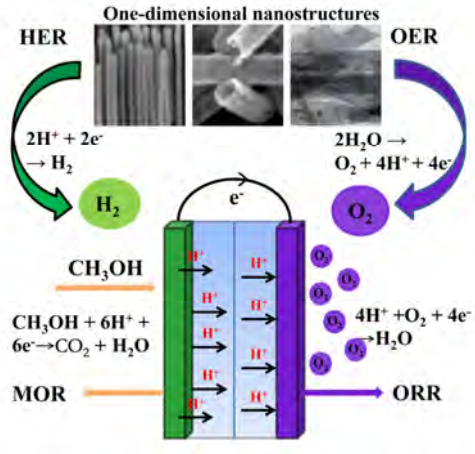

This overview summarizes the recent advances in one-dimensional metal nanostructures for energy electrocatalysis, including the main reactions in direct methanol fuel cells and water splitting.

Chin. J. Catal., 2019, 40: 23–37 doi: 10.1016/S1872-2067(18)63161-4

Transition metal-nitrogen sites for electrochemical carbon dioxide reduction reaction

Chengcheng Yan, Long Lin, Guoxiong Wang *, Xinhe Bao *
Dalian Institute of Chemical Physics, Chinese Academy of Sciences; University of Chinese Academy of Sciences

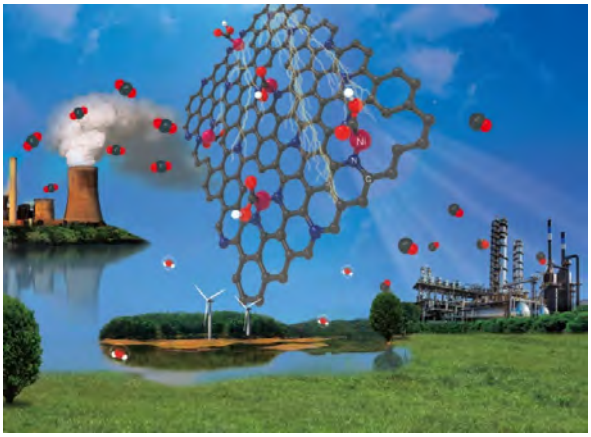

Metal-nitrogen sites constituted of earth abundant elements with maximum atom-utilization efficiency have emerged as promising catalysts for electrochemical CO_2 reduction reaction.

Communication

Chin. J. Catal., 2019, 40: 38–42 doi: 10.1016/S1872-2067(18)63190-0

A hydrated amorphous iron oxide nanoparticle as active water oxidation catalyst

Zheng Chen, Qinge Huang, Baokun Huang, Fuxiang Zhang *, Can Li *
Dalian Institute of Chemical Physics, Chinese Academy of Sciences

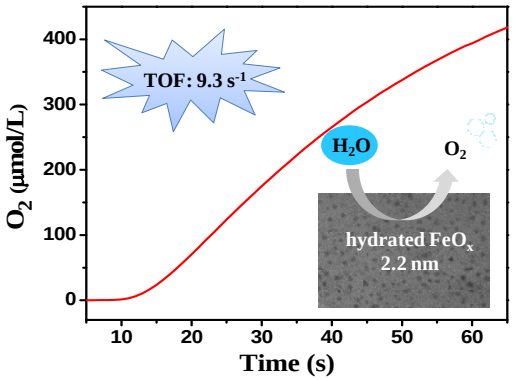

$$2S_2O_8^{2-} + 2H_2O \xrightarrow[Ru(bpy)_3^{2+},\ h\nu]{FeO_x} O_2\uparrow + 4H^+ + 4SO_4^{2-}$$

A hydrated amorphous iron oxide nanoparticle exhibits high water oxidation activity with TOF of 9.3 s^{-1} in the photocatalytic $Ru(bpy)_3^{2+}$-$Na_2S_2O_8$.

Articles

Chin. J. Catal., 2019, 40: 43–51 doi: 10.1016/S1872-2067(18)63175-4

Synthesis of silk-like FeS_2/NiS_2 hybrid nanocrystals with improved reversible oxygen catalytic performance in a Zn-air battery

Jing Jin, Jie Yin, Pinxian Xi *
Lanzhou University

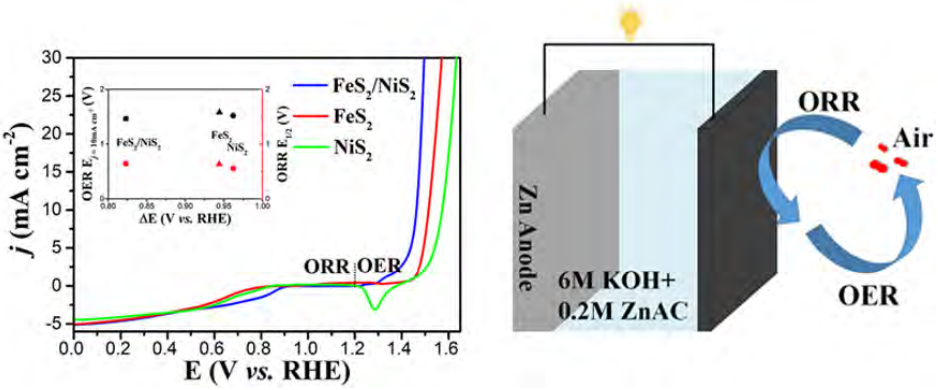

Herein, an efficient liquid exfoliation strategy was designed for producing silk-like FeS_2/NiS_2 hybrid nanocrystals with enhanced reversible oxygen catalytic performance that displayed excellent properties for Zn-air batteries.

Chin. J. Catal., 2019, 40: 52–59 doi: 10.1016/S1872-2067(18)63167-5

Eco-friendly synthesis of high silica zeolite Y with choline as green and innocent structure-directing agent

Dawei He, Danhua Yuan, Zhijia Song, Yunpeng Xu *, Zhongmin Liu *
Dalian Institute of Chemical Physics, Chinese Academy of Sciences; University of Chinese Academy of Sciences

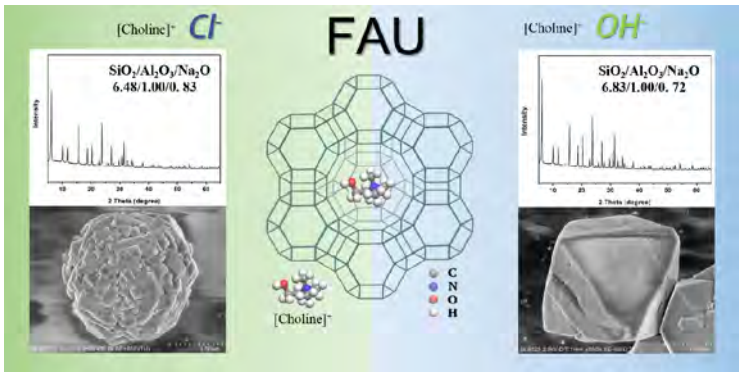

Choline chloride or choline hydroxide was used as an eco-friendly and nontoxic organic structure-directing agent (OSDA) for the synthesis of high silica zeolite Y with SiO_2/Al_2O_3 ratios of 6.5–6.8.

Chin. J. Catal., 2019, 40: 60–69 doi: 10.1016/S1872-2067(18)63170-5

Construction of 2D-2D TiO_2 nanosheet/layered WS_2 heterojunctions with enhanced visible-light-responsive photocatalytic activity

Yongchuan Wu, Zhongmin liu, Yaru Li, Jitao Chen, Xixi Zhu, Ping Na *
Tianjin University; College of Chemistry and Chemical Engineering; Shandong University of Science and Technology

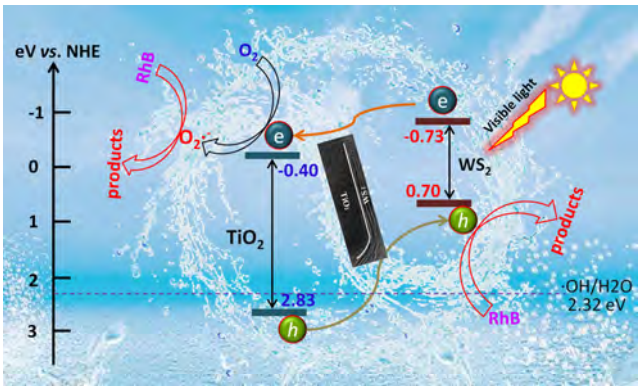

The 2D-2D TNS/WS_2 heterojunction was successfully constructed by in-situ growing the layered WS_2 on the surface of TiO_2 nanosheet. The 2D-2D nanointerfaces boosted the separation of photogenerated carriers, thereby resulting in a higher photocatalytic activity.

Chin. J. Catal., 2019, 40: 70–79 doi: 10.1016/S1872-2067(18)63160-2

Enhanced photocatalytic Cr(VI) reduction and diclofenac sodium degradation under simulated sunlight irradiation over MIL-100(Fe)/g-C_3N_4 heterojunctions

Xuedong Du, Xiaohong Yi, Peng Wang, Jiguang Deng *, Chong-chen Wang *
Beijing University of Civil Engineering and Architecture; Beijing University of Technology

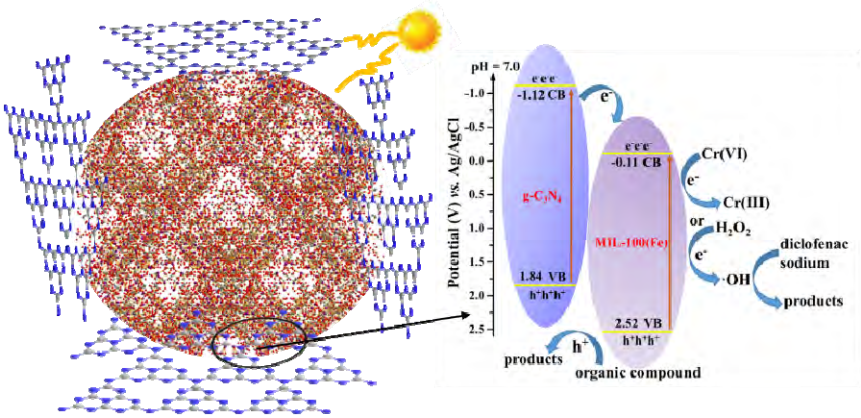

The MIL-100(Fe)/g-C_3N_4 hybrids show high photocatalytic activity under simulated sunlight and can reduce Cr(VI) to Cr(III) and decompose diclofenac sodium effectively.

Chin. J. Catal., 2019, 40: 80–94 doi: 10.1016/S1872-2067(18)63172-9

Fast electron transfer and enhanced visible light photocatalytic activity by using poly-o-phenylenediamine-modified AgCl/g-C_3N_4 nanosheets

Linlin Sun, Chongyang Liu, Jinze Li, Yaju Zhou, Huiqin Wang *, Pengwei Huo *, Changchang Ma, Yongsheng Yan
Jiangsu University

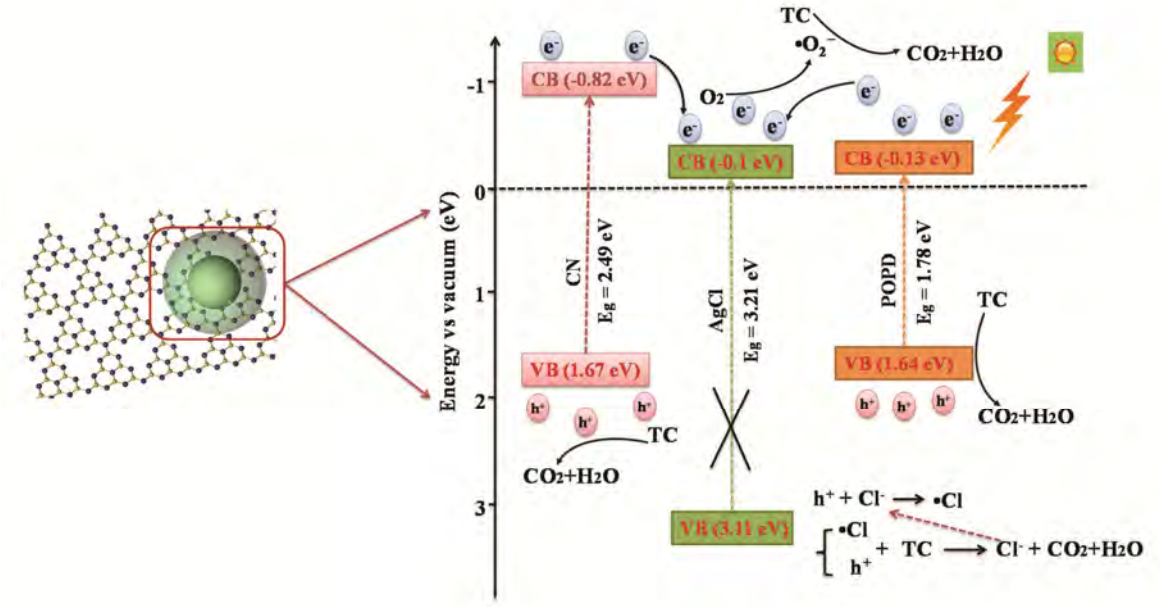

The degradation efficiency of tetracycline over PoPD/AgCl/CN composites synthesized by precipitation reaction and photoinitiated polymerization approach was three times higher than that over pure CN; $•O_2^-$ and h^+ are the main reactive species in the case of PoPD/AgCl/CN.

Chin. J. Catal., 2019, 40: 95–104 doi: 10.1016/S1872-2067(18)63184-5

Improving the denitration performance and K-poisoning resistance of the V_2O_5-WO_3/TiO_2 catalyst by Ce^{4+} and Zr^{4+} co-doping

Jun Cao, Xiaojiang Yao *, Fumo Yang, Li Chen, Min Fu *, Changjin Tang, Lin Dong
Chongqing Technology and Business University; Chongqing Institute of Green and Intelligent Technology, Chinese Academy of Sciences; Sichuan University; Nanjing University

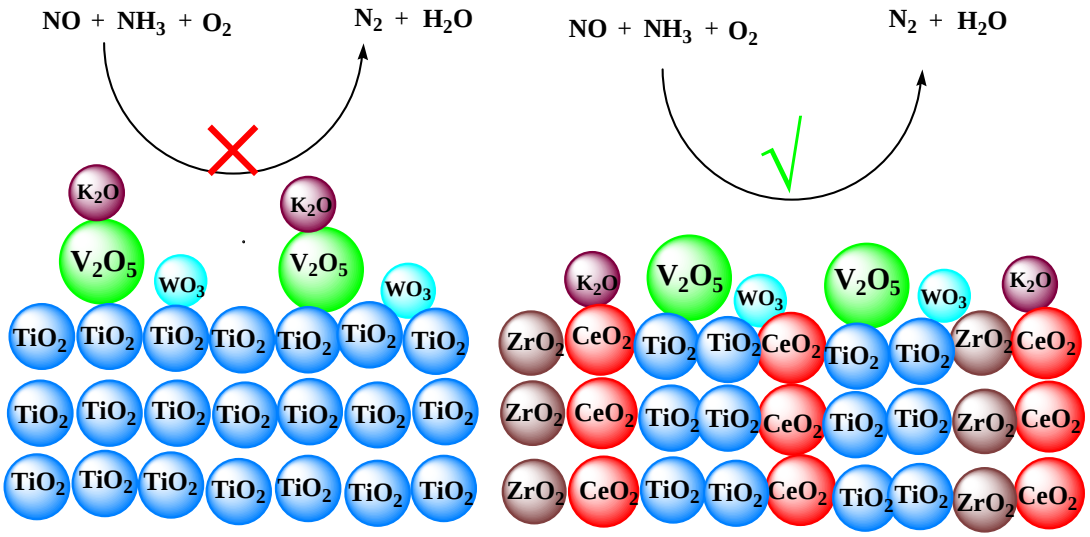

Co-doping of Ce^{4+} and Zr^{4+} enhances the denitration performance and K-poisoning resistance of V_2O_5-WO_3/TiO_2 catalyst because more K atoms can be combined with Ce^{4+} to yield the better protection of active vanadium species.

Chin. J. Catal., 2019, 40: 105–113 doi: 10.1016/S1872-2067(18)63164-X

Synergistic effects of CuO and Au nanodomains on Cu_2O cubes for improving photocatalytic activity and stability

Denghui Jiang, Yuegang Zhang, Xinheng Li *
Lanzhou Institute of Chemical Physics (LICP), Chinese Academy of Sciences; Central South University; Suzhou Institute of Nano-tech and Nano-bionics, Chinese Academy of Sciences

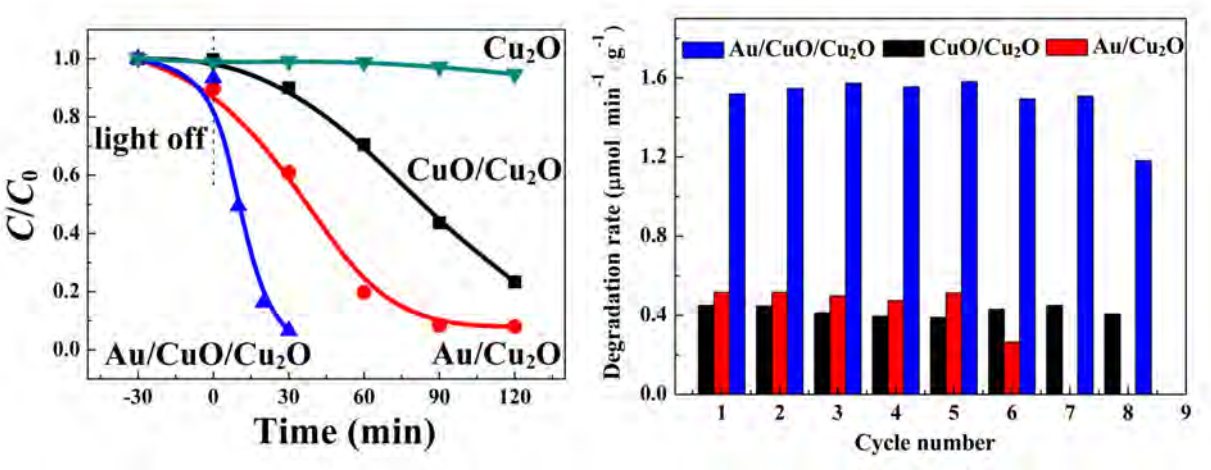

Au/CuO/Cu_2O catalysts were synthesized by sequential surface oxidative and reductive deposition on Cu_2O surfaces improving both the photocatalytic activity and stability of Cu_2O.

Chin. J. Catal., 2019, 40: 114–123 doi: 10.1016/S1872-2067(18)63192-4

A highly stable and active mesoporous ruthenium catalyst for ammonia synthesis prepared by a $RuCl_3/SiO_2$-templated approach

Yaping Zhou, Yongcheng Ma, Guojun Lan, Haodong Tang, Wenfeng Han, Huazhang Liu, Ying Li *
Zhejiang University of Technology; Sichuan Huadi Construction Engineering Co., Ltd.

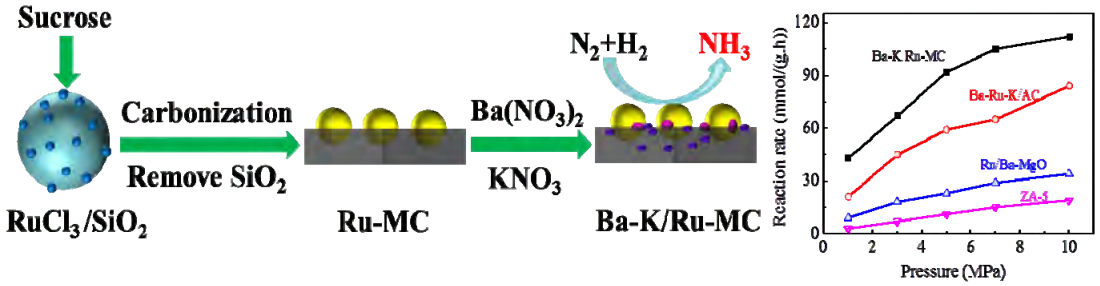

Semi-embedded Ru-MC has stable Ru NPs and strong interaction between Ru and C that promote the catalytic performance for ammonia synthesis.

中国科学院科学出版基金资助出版

催化学报 Chinese Journal of Catalysis

月刊 SCI收录 2019年1月 第40卷 第1期

目 次

学术讨论

1
关于双光束红外光谱在气固相多相催化反应实时原位表征中气相校正的讨论
Frederic Meunier

综 述

4
一维纳米材料在能源电催化中的研究进展
李苹，陈卫

23
过渡金属-氮活性位点在二氧化碳电化学还原反应中的应用
阎程程，林龙，汪国雄，包信和

快 讯

38
水合状态的无定形氧化铁作为高效水氧化催化剂的研究
陈政，黄清娥，黄保坤，章福祥，李灿

论 文

43
可逆氧催化性能提升的FeS_2/NiS_2纳米复合物的合成及其在锌空电池中的应用
靳晶，殷杰，刘瀚文， 席聘贤

52
以胆碱为绿色无毒有机结构导向剂合成高硅Y型分子筛
贺大威，袁丹华，宋智甲，徐云鹏，刘中民

60
构建2D-2D TiO_2纳米片/层状WS_2异质结用以增强可见光响应光催化活性
吴勇川，刘中敏，李亚茹，陈继涛，祝熙熙，那平

70
模拟太阳光照射下MIL-100(Fe)/g-C_3N_4异质结光催化Cr(VI)还原和双氯芬酸钠降解
杜雪冬，衣晓虹，王鹏，邓积光，王崇臣

80
聚邻苯二胺修饰AgCl/g-C_3N_4纳米片复合光催化剂的制备及性能研究
孙林林，刘重阳，李金择，周亚举，王会琴，霍鹏伟，马长畅，闫永胜

95
Ce^{4+}，Zr^{4+}共掺杂提高V_2O_5-WO_3/TiO_2催化剂脱硝性能及抗K中毒能力
曹俊，姚小江，杨复沫，陈丽，傅敏，汤常金，董林

105
CuO和Au纳米结构协同增强Cu_2O立方体光催化活性和稳定性
蒋登辉，张跃钢，李鑫恒

114
以$RuCl_3/SiO_2$为模板制备的高性能镶嵌式钌基氨合成催化剂
周亚萍，马永承，蓝国钧，唐浩东，韩文锋，刘化章，李瑛

相关信息

124 《催化学报》第五届编辑委员会
128 Guide for Authors
135 《催化学报》作者指南

英文全文电子版(国际版)由Elsevier出版社在ScienceDirect上出版
http://www.sciencedirect.com/science/journal/18722067
http://www.elsevier.com/locate/chnjc
www.cjcatal.org
在线投审稿网址
https://mc03.manuscriptcentral.com/cjcatal

available at www.sciencedirect.com

ScienceDirect

journal homepage: www.elsevier.com/locate/chnjc

Article

Enhanced photocatalytic Cr(VI) reduction and diclofenac sodium degradation under simulated sunlight irradiation over MIL-100(Fe)/g-C_3N_4 heterojunctions

Xuedong Du [a], Xiaohong Yi [a], Peng Wang [a], Jiguang Deng [b,*], Chong-chen Wang [a,#]

[a] *Beijing Key Laboratory of Functional Materials for Building Structure and Environment Remediation, Beijing University of Civil Engineering and Architecture, Beijing 100044, China*

[b] *Department of Chemistry and Chemical Engineering, College of Environmental and Energy Engineering, Beijing University of Technology, Beijing 100022, China*

ARTICLE INFO

Article history:
Received 24 July 2018
Accepted 12 September 2018
Published 5 January 2019

Keywords:
MIL-100(Fe)
g-C_3N_4
Heterojunction
Cr(VI) reduction
Diclofenac sodium

ABSTRACT

Metal-organic framework MIL-100(Fe) and g-C_3N_4 heterojunctions (MG-*x*, *x* = 5%, 10%, 20%, and 30%, *x* is the mass fraction of MIL-100(Fe) in the hybrids) were facilely fabricated through ball-milling and annealing, and characterized by powder X-ray diffraction, Fourier transform infrared spectroscopy, thermogravimetric analysis, transmission electron microscopy, UV-visible diffuse-reflectance spectrometry, and photoluminescence emission spectrometry. The photocatalytic activities of the series of MG-*x* heterojunctions toward Cr(VI) reduction and diclofenac sodium degradation were tested upon irradiation with simulated sunlight. The influence of different organic compounds (ethanol, citric acid, oxalic acid, and diclofenac sodium) as hole scavengers and the pH values (2, 3, 4, 6, and 8) on the photocatalytic activities of the series of MG-*x* heterojunctions was investigated. MG-20% showed superior photocatalytic Cr(VI) reduction and diclofenac sodium degradation performance than did the individual MIL-100(Fe) and g-C_3N_4 because of the improved separation of photoinduced electron-hole charges, which was clarified via photoluminescence emission and electrochemical data. Moreover, the MG-*x* exhibited good reusability and stability after several runs.

1. Introduction

Among toxic heavy metal ions, hexavalent chromium (Cr(VI)) is a mutagenic and carcinogenic contaminant that is found in surface water and groundwater, as it is widely utilized in the electroplating, leather tanning, printing, polishing, and pigment industries [1–3]. Up to now, photocatalytic reduction of Cr(VI) to Cr(III) has been a hot topic of research [4–10], therefore, it is a great challenge to develop novel photocatalysts with efficient visible-light absorption and excellent stability

* Corresponding author. Tel/Fax: +86-10-67391767; E-mail: jgdeng@bjut.edu.cn
# Corresponding author. Tel/Fax: +86-010-61209186; E-mail: wangchongchen@bucea.edu.cn

This work was supported by the National Natural Science Foundation of China (51578034, 51878023), the Great Wall Scholars Training Program Project of Beijing Municipality Universities (CIT&TCD20180323), the Project of Construction of Innovation Teams and Teacher Career Development for Universities and Colleges Under Beijing Municipality (IDHT20170508), the Beijing Talent Project (2017A38), the Fundamental Research Funds for Beijing Universities (X18075/X18076/X18124/X18125/X18276), and the Scientific Research Foundation of Beijing University of Civil Engineering and Architecture (KYJJ2017033/KYJJ2017008).
DOI: 10.1016/S1872-2067(18)63160-2 | http://www.sciencedirect.com/science/journal/18722067 | Chin. J. Catal., Vol. 40, No. 1, January 2019

[8,11]. Among the various photocatalysts, graphitic carbon nitride (g-C_3N_4) is a good, metal-free photocatalyst that possesses appealing features like π-conjugated electronic structure, high chemical stability, and earth abundance [12,13]. However, g-C_3N_4 has some disadvantages, such as high recombination probability of the photogenerated electron-hole pairs due to hybridization of the N 2*p* and C 2*p* states in the conduction band (CB) and unavoidably disordered structure or defects [14–16] and low surface area resulting from the bulk structure [17–19]. These disadvantages lead to the low photocatalytic activity for Cr(VI) reduction or organic pollutant degradation. Recently, synthesis of g-C_3N_4 composites with different materials, such as g-C_3N_4/Bi_2WO_6 [20], g-C_3N_4/SiW_{11} [21], g-C_3N_4/$Zn_3V_2O_7(OH)_2(H_2O)_2$ [22], WO_3/g-C_3N_4 [23], g-C_3N_4/Ag_2O [24], and g-PAN/g-C_3N_4 [25], has been identified to be an efficient way to improve the photocatalytic reduction efficiency.

Recently, the application of metal-organic frameworks (MOFs) in heterogeneous photocatalysis under UV/visible/UV-vis irradiation for water splitting and CO_2 & Cr(VI) reduction by using photogenerated electrons as well as the degradation of organic pollutants based on holes has become widespread [8,26–30]. The photocatalytic performance of composites containing g-C_3N_4 and MOFs has been widely reported. For example, ZIF-9(Co)/g-C_3N_4 exhibited multiple functions in both CO_2 adsorption and high photocatalytic activity for CO_2 reduction [31]. UiO-66(Zr)/g-C_3N_4 demonstrated efficient photocatalytic hydrogen production because of the heterojunctions [32]. MIL-125(Ti)/g-C_3N_4, MIL-53(Al)/g-C_3N_4, and MIL-100(Fe)/g-C_3N_4 exhibited highly efficient photocatalytic performance toward rhodamine B degradation in aqueous solution under visible-light irradiation [12,33,34]. ZIF-8(Zn)/g-C_3N_4 is a bifunctional material that shows efficient adsorption and facilitates sunlight-induced photocatalytic degradation of tetracycline [35]. ZIF-NC/g-C_3N_4 composites exhibit enhanced photocatalytic activity for bisphenol A degradation with peroxymonosulfate under visible-light irradiation [36]. Moreover, MIL-53(Fe)/g-C_3N_4 had improved photocatalytic efficiency for Cr(VI) reduction [37].

In this work, MIL-100(Fe)/g-C_3N_4 hybrids were synthesized through ball-milling and annealing for photocatalytic Cr(VI) reduction under different conditions. Both g-C_3N_4 and MIL-100(Fe) showed photocatalytic performance, but each material when used individually exhibited limited photocatalytic efficiency due to the high charge recombination rate and limited light absorption ability. The MIL-100(Fe)/g-C_3N_4 hybrids obtained by combining MIL-100(Fe) with g-C_3N_4 demonstrated outstanding photocatalytic performance for Cr(VI) reduction under simulated sunlight, along with good stability and reusability.

2. Experimental

2.1. Materials

All chemicals including urea (CH_4N_2O, USP grade, Amresco), iron powder (Fe, 99%, J&k Scientific Ltd.), benzene-1,3,5-tricarboxylic acid (H_3BTC, $C_9H_6O_6$, 99%, J&k Scientific Ltd.), nitric acid (HNO_3, analytical grade, Sinopharm Chemical Reagent Co., Ltd.), hydrofluoric acid (HF, analytical grade, Sinopharm Chemical Reagent Co., Ltd.), potassium dichromate ($K_2Cr_2O_7$, analytical grade, Sinopharm Chemical Reagent Co., Ltd.), diclofenac sodium ($C_{14}H_{10}Cl_2NNaO_2$, 98%, J&k Scientific Ltd.), hydrogen peroxide (H_2O_2, 30 wt%, Sinopharm Chemical Reagent Co., Ltd.), oxalic acid ($H_2C_2O_4$, analytical grade, Sinopharm Chemical Reagent Co., Ltd.), citric acid monohydrate ($C_6H_8O_7{\cdot}H_2O$, 99%, J&k Scientific Ltd.), sodium acetate ($C_2H_3O_2Na$, analytical grade, Sinopharm Chemical Reagent Co., Ltd.), and acetonitrile ($C_2H_3N{\cdot}H_2O$, LC-MS grade, J&k Scientific Ltd.) were commercially available and used without further purification.

2.2. Preparation of MIL-100(Fe)/g-C_3N_4 hybrids

g-C_3N_4 was prepared by calcination with urea as the precursor [33]. Briefly, 10.0 g of urea was placed in a porcelain crucible with a cover, moved into a muffle furnace, and heated at 500 °C for 4 h. The obtained yellow powder was collected for further use. Crude g-C_3N_4 powder (1.0 g) was dispersed in 200.0 mL deionized H_2O by sonication for 6 h. Then, pure g-C_3N_4 was obtained by centrifuging the supernatant at 6000 rpm for 10 min and dried at 60 °C for 6 h.

MIL-100(Fe) was synthesized according to the procedure reported by Horcajada and coworkers [38]. A mixture of 0.139 g Fe^0, 0.344 g H_3BTC, 0.1 mL HF, 0.1 mL HNO_3, and 10.0 mL H_2O with a molar ratio of 1.0:0.66:2.0:1.2:280 was sealed in a 25.0 mL Teflon-lined autoclave and heated at 150 °C for 6 d. The light-orange MIL-100(Fe) was collected by filtration, washed with deionized water, and finally dried in an oven at 60 °C for 2 h.

The MIL-100(Fe)/g-C_3N_4 heterojunctions (MG-*x*, *x* = 5%, 10%, 20%, and 30%, *x* is the mass fraction of MIL-100 in hybrids) were fabricated by ball-milling, followed by thermal treatment of the mixture of g-C_3N_4 and MIL-100(Fe). In a typical procedure, a certain amount of MIL-100(Fe) and g-C_3N_4 powders was mixed in a stainless-steel pot and ground for 20 min using a ball mill. The ground mixture was then thermally treated at 300 °C for 2 h in a tube furnace under N_2 atmosphere to produce a series of MIL-100(Fe)/g-C_3N_4 (MG-*x*) heterojunctions. For comparison, pristine g-C_3N_4 and MIL-100(Fe) were also thermally treated under the same conditions as those for the MG-*x* hybrids.

2.3. Characterization

Powder X-ray diffraction (PXRD) patterns of the samples were obtained with a Dandong Haoyuan DX-2700B diffractometer in the range of 2θ = 5°–50° with Cu K_α radiation. Thermogravimetric analyses (TGA) were performed in the range of 90–800 °C in an air stream at a heating rate of 10 °C/min on a DTU-3c thermal analyzer using α-Al_2O_3 as a reference. Fourier transform infrared (FT-IR) spectra were recorded using KBr pellets on a Nicolet 6700 spectrometer in the range of 4000–400 cm^{-1}. UV-visible diffuse-reflectance spectra (UV-vis

DRS) of the solid samples were measured in the range of 200–800 nm on a Perkin Elmer Lambda 650S spectrophotometer, in which barium sulfate ($BaSO_4$) was used as the standard with 100% reflectance. Photoluminescence (PL) emission spectra were recorded on a Hitachi F-7000 spectrophotometer across wavelengths ranging from 400 to 600 nm at room temperature, with an excitation wavelength of 320 nm. The surface area of the sample was calculated from N_2 adsorption-desorption isotherms measured on a BELSORP-mini II surface area analyzer at –196 °C using the Brunauer-Emmett-Teller (BET) nitrogen adsorption method. The morphology of the samples was observed using a Hitachi HT7700 transmission electron microscope (TEM) operating at an acceleration voltage of 120 kV. X-ray photoelectron spectroscopy (XPS) measurements were performed with Thermo ESCALAB 250XI.

2.4. Electrochemical measurements

Electrochemical measurements were conducted using a Metrohm Autolab PGSTAT204 electrochemical station in a typical three-electrode mode with 0.2 mol/L Na_2SO_4 aqueous solution (pH = 6.8) as the electrolyte. A Pt electrode and a saturated Ag/AgCl electrode were used as the counter electrode and reference electrode, respectively. Powder samples of 5.0 mg MIL-100(Fe) or g-C_3N_4 were mixed sufficiently with 400.0 μL ethanol/Nafion (v/v = 19/1) under sonication for 30 min to prepare the working electrodes. The prepared slurry (10.0 μL) was drop-cast onto the conductive side of a Fluorine-doped Tin Oxide (FTO) substrate (1.0 cm × 1.0 cm), and then dried at 80 °C for 30 min. This step was repeated five times to ensure uniform coverage of MIL-100(Fe) or g-C_3N_4 on the FTO substrate for obtaining the desired working electrodes.

2.5. Photocatalytic experiment

The photocatalytic Cr(VI) reduction experiment was carried out at 25 °C in a 300 mL quartz reactor containing 100.0 mg of the photocatalyst and 200.0 mL of 10.0 ppm Cr(VI) aqueous solution, and the solution pH was adjusted to 2.0–8.0 with 0.2 mol/L H_2SO_4 or 0.2 mol/L NaOH solution. After stirring for 60 min to achieve adsorption-desorption equilibrium, the suspensions were irradiated by a 300 W xenon lamp (Beijing Aulight Co., Ltd.). The spectrum of the light source is shown in Fig. S1 (Supporting Information). During illumination, 2.5 mL of the suspension was taken from the reactor at specific time intervals and centrifuged to separate the photocatalyst. The Cr(VI) content in the supernatant was determined colorimetrically at 540 nm using the diphenylcarbazide method with a Yuanxi UV-5200PC UV-vis spectrophotometer [39].

The photocatalytic degradation performance of the MG-x nanocomposites toward diclofenac sodium was also tested. In a typical experiment, 100.0 mg of photocatalyst powder was dispersed in 200.0 mL diclofenac sodium aqueous solution (0.1 mmol/L). The suspension was stirred in the dark for 60 min to achieve adsorption–desorption equilibrium, and then, hydrogen peroxide (50.0 μL) was added to the suspension before turning on the light. A 300 W xenon lamp (Beijing Aulight Co. Ltd.) was used as the light source. During the photocatalytic degradation, the samples were collected at regular time intervals using a 0.22-mm syringe filter to remove the photocatalyst particles before analysis. An Acquity UPLC H-Class (Waters) system was used to detect the residual concentration of diclofenac sodium after the photocatalytic degradation. The analytes were separated on a C18 (1.7 μm, 2.1 mm × 50 mm) column in a UPLC system equipped with a TUV detector. Aqueous sodium acetate solution (0.015 mol/L) and acetonitrile were used as mobile phases A and B, respectively. The gradient was programmed as follows: 0–0.5 min, 0–0% B; 0.5–1 min, 0–48% B; 1–2 min, 48–48% B; 2–2.5 min, 48–0% B. The column temperature was maintained at 40 °C.

3. Results and discussion

3.1. Characterization

The PXRD patterns of the parent materials and heterojunctions are illustrated in Fig. 1. The PXRD patterns of MIL-100(Fe) were consistent with those reported in the literature (Fig. S2) [38,40], demonstrating that the prepared MIL-100(Fe) was pure and well crystallized. The typical interlayer-stacking peak (002) at 2θ = 27.2° corresponded to an interlayer distance of ~0.32 nm for g-C_3N_4 [41,42]. The PXRD patterns of the MG-x composites matched well with the corresponding peaks of g-C_3N_4 and MIL-100(Fe), implying their successful combination. More importantly, no sign of a new phase in the MG-x hybrids was observed after annealing; the characteristic peaks at 6.2°, 10.2°, 11.0°, and 20.0° attributed to MIL-100(Fe) became more evident with increasing mass content in the MG-x samples. The unchanged backbones of g-C_3N_4 and MIL-100(Fe) in the MG-x hybrids were further revealed by the identical FTIR spectra, as shown in Fig. 2. As expected, the same characteristic absorption peaks were observed for g-C_3N_4 and MG-x hybrids, except for the low MIL-100(Fe) content in the MG-x samples. The texture of MG-20% hybrids was selected for observation in the TEM and HRTEM images, as shown in

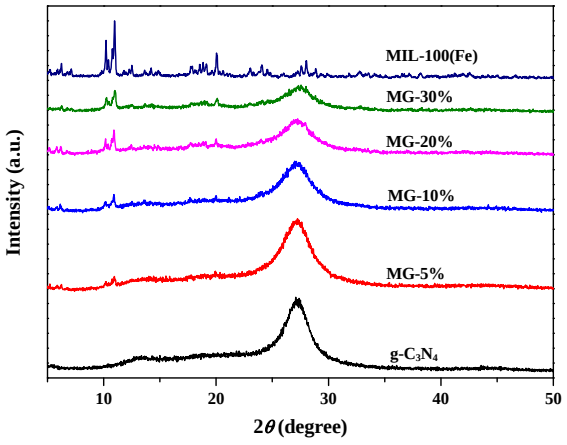

Fig. 1. XRD patterns of g-C_3N_4, MG-x (x = 5%, 10%, 20%, and 30%) hybrids, and MIL-100(Fe).

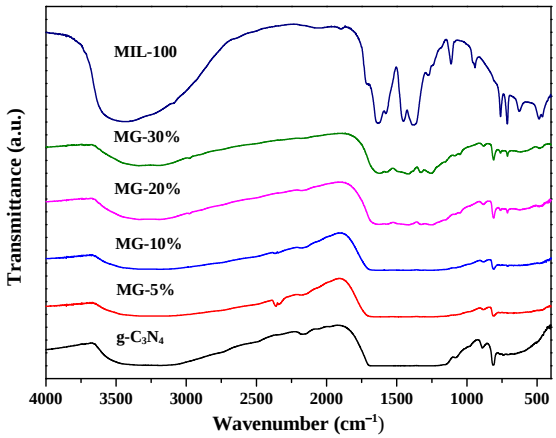

Fig. 2. FTIR spectra of g-C_3N_4, MG-*x* (*x* = 5%, 10%, 20%, and 30%) hybrids, and MIL-100(Fe).

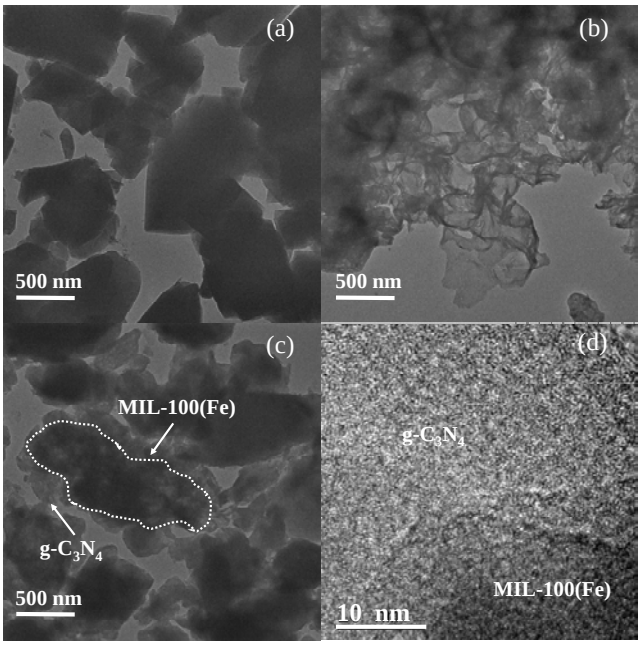

Fig. 3. TEM images of (a) pure MIL-100(Fe), (b) pure g-C_3N_4, and (c) MG-20%, and (d) HRTEM image of MG-20%.

Fig. 3. For comparison, the TEM images of pure MIL-100(Fe) and g-C_3N_4 were also included. MIL-100(Fe) (Fig. 3(a)) displayed a polygonal structure [34], and g-C_3N_4 samples (Fig. 3(b)) exhibited aggregated, slate-like, and smooth particles with lamellar structures [33]. It could also be clearly observed that the g-C_3N_4 nanosheets adhered strongly to the edges of MIL-100(Fe) (Fig. 3(c)). High-resolution TEM images (Fig. 3(d)) could not be obtained as g-C_3N_4 and MIL-100(Fe) were solids with low crystalline quality [32]. TGA revealed that the thermal stability of MG-*x* decreased with an increase in the MIL-100(Fe) content in the MG sample, as shown in Fig. 4, and the residual weight further confirmed the different MIL-100(Fe) contents in the MG-*x* samples.

Fig. 5 presents the XPS survey spectrum and the high-resolution XPS spectra of MG-20%. The XPS survey spectrum (Fig. 5(a)) shows that C, N, O, and Fe exist in MG-20%. Fig.

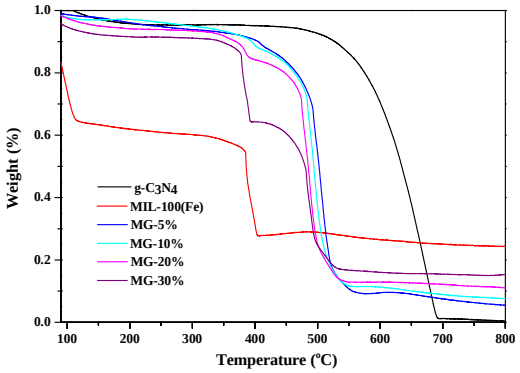

Fig. 4. Thermal analysis of g-C_3N_4, MG-*x* (*x* = 5%, 10%, 20%, and 30%) hybrids, and MIL-100(Fe).

5(b) shows the C 1*s* XPS spectrum of MG-20%, in which the peaks at 284.3 eV/288.2 eV and 285.3 eV can be attributed to the sp^2-bonded carbon (C–C bond)/C–H bond and C–N present in the g-C_3N_4, respectively [33,37], while the peaks at 284.9 and 288.7 eV can be ascribed to benzoic rings and C=O bonds of the H_2bdc ligand in MIL-100(Fe) [43]. Four binding energies in the N 1*s* region (Fig. 5(c)) can be observed, which can be ascribed to the C–N–C (398.7 eV), N–$(C)_3$ (400.1 eV), and N–H groups (401.3 eV), and the charging effects (404.9 eV), respectively [44]. The spectrum of MG-20% (Fig. 5(d)) exhibits two O 1*s* peaks at 531.2 and 532.2 eV, which are related to the Fe–O bonds of MG-20% and the oxygen components of the H_2bdc ligand, respectively [45]. Furthermore, the Fe 2*p* spectrum in Fig. 5(e) has two peaks at 712.5 and 725.4 eV, which can be assigned to Fe $2p_{3/2}$ and Fe $2p_{1/2}$, respectively [46]. These results clearly imply that the MG-20% photocatalyst is successfully fabricated. The UV-vis DRS spectra of g-C_3N_4, MIL-100(Fe), and MG-*x* are shown in Fig. 6(a). The band-gap energy (E_g) and band-edge wavelength (λ_g) of g-C_3N_4, MIL-100(Fe), and MG-*x* can be estimated using Eqs. (1) and (2), respectively [47].

$$Ahv = k(hv - E_g)^{1/n} \quad (1)$$

$$\lambda_g = 1240/E_g \quad (2)$$

where *k* represents a constant, and *n* is determined by the type of optical transition of a semiconductor. The results reveal that the E_g values of g-C_3N_4, MG-5%, MG-10%, MG-20%, MG-30%, and MIL-100(Fe) are 2.96, 2.87, 2.83, 2.80, 2.77, and 2.63 eV, respectively, and the band gaps tend to become narrow with an increase in the MIL-100(Fe) content. The PL spectra of g-C_3N_4 and MG-20% at an excitation wavelength of 320 nm are demonstrated in Fig. 7. The PL intensity of MG-20% at the 440 nm peak is weaker than that of pure g-C_3N_4, implying that the recombination rate of photogenerated electrons and holes decreases in case of MG-20% [48,49].

3.2. Photocatalytic activity

Before the photocatalytic reduction experiments, the adsorption abilities of the samples were tested. As shown in Fig. 8(a), the adsorption capacity of g-C_3N_4 and MG-*x* hybrids toward $Cr_2O_7^{2-}$ was about 5%, while MIL-100(Fe) showed higher

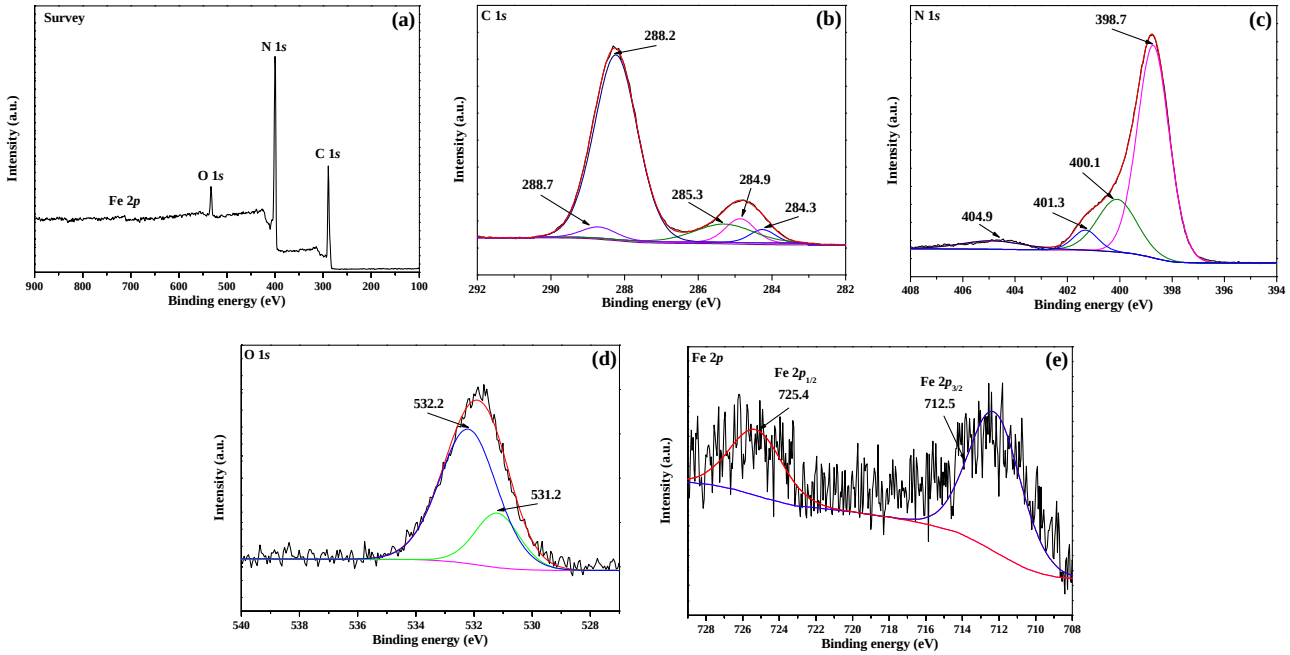

Fig. 5. XPS spectra of the MG-20% hybrid. (a) Survey scan; (b) C 1s; (c) N 1s; (d) O 1s; (e) Fe 2*p*.

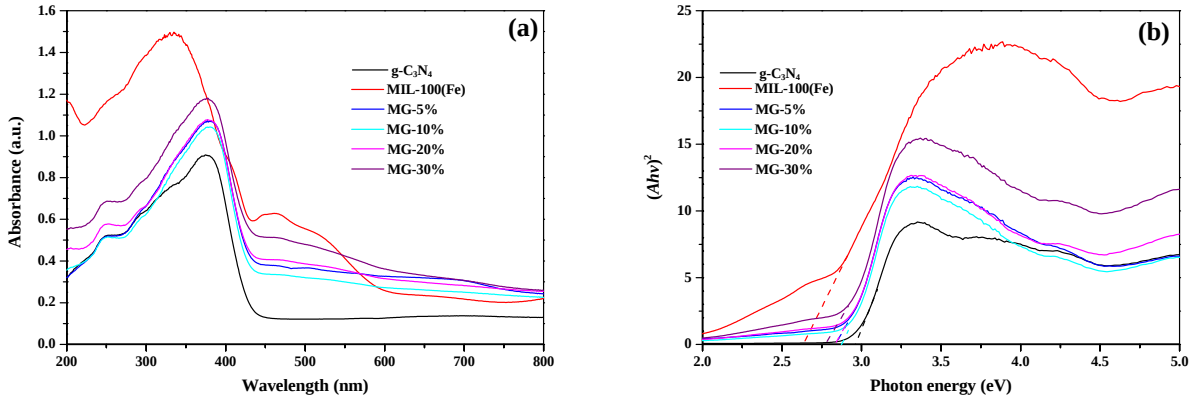

Fig. 6. (a) UV-vis spectra and (b) $(Ahv)^2$ versus photon energy (hv) plots for g-C_3N_4, MG-x (x = 5%, 10%, 20%, and 30%) hybrids, and MIL-100(Fe).

adsorption activity toward $Cr_2O_7^{2-}$ (~20%) because of its positive surface at pH 2.0 [50,51]. The photocatalytic Cr(VI) reduction performance over MG-x (x = 5%, 10%, 20%, and 30%) under simulated sunlight irradiation was evaluated, as illustrated in Fig. 8(a). All MG-x hybrids exhibited higher photocatalytic activities than those of pure g-C_3N_4 and MIL-100(Fe) owing to the synergistic effect between g-C_3N_4 and MIL-100(Fe). The MG-20% hybrid demonstrated the best photocatalytic activity, evidenced by its Cr(VI) reduction (97%) efficiency within 80 min. The kinetic curves for the photocatalytic reduction of Cr(VI) over MG-x (5%, 10%, 20%, and 30%) photocatalysts were plotted to the pseudo-first order model ($\ln(C/C_0) = kt$), and the values of k are shown in Fig. 8(b). The order of the Cr(VI) reduction rates for the as-prepared photocatalysts is as follows: MG-20% (0.037 min^{-1}) > MG-10% (0.028 min^{-1}) > MG-30% (0.026 min^{-1}) > MG-5% (0.023 min^{-1}) > g-C_3N_4 (0.016 min^{-1}) > MIL-100(Fe) (0.012 min^{-1}). Appropriate introduction of MIL-100(Fe) into g-C_3N_4 will not only be beneficial for charge transfer at the heterojunction interfaces, but also improve visible-light harvesting (Fig. 6(a)). However, excess g-C_3N_4 may decrease the quality of effective heterointerfaces in MG-x, which would be unfavorable for charge transfer at the heterointerfaces [32,33,52].

During the redox process, the Cr(VI) reduction rate over the photocatalyst is greatly influenced by the pH of the aqueous solution. The reduction efficiencies of Cr(VI) over MG-20% at different pH values are shown in Fig. 9(a). The reduction ratio decreased rapidly with increasing pH (98%, 79%, 29%, 15%, and 9% at pH 2, 3, 4, 6, and 8, respectively). Under acidic conditions, the photocatalytic Cr(VI) reaction follows Eq. (4), and the abundant H^+ further facilitates the conformation change from Cr(VI) to Cr(III) [8]. However, under alkaline conditions, CrO_4^{2-} is predominant, leading to a reaction as expressed in Eq. (6) [8]. Moreover, the $Cr(OH)_3$ precipitate formed at pH > 6 covers the

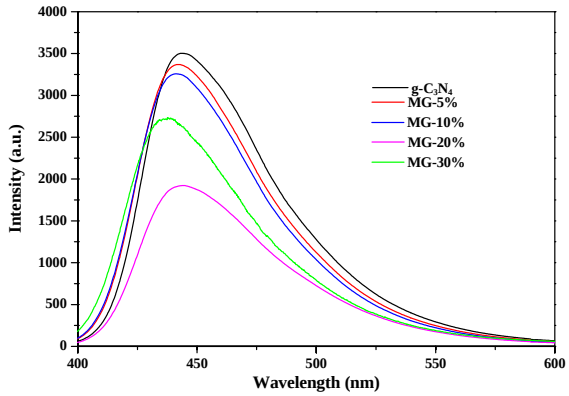

Fig. 7. Photoluminescence spectra of g-C_3N_4 and MG-*x* (*x* = 5%, 10%, 20%, and 30%) hybrids.

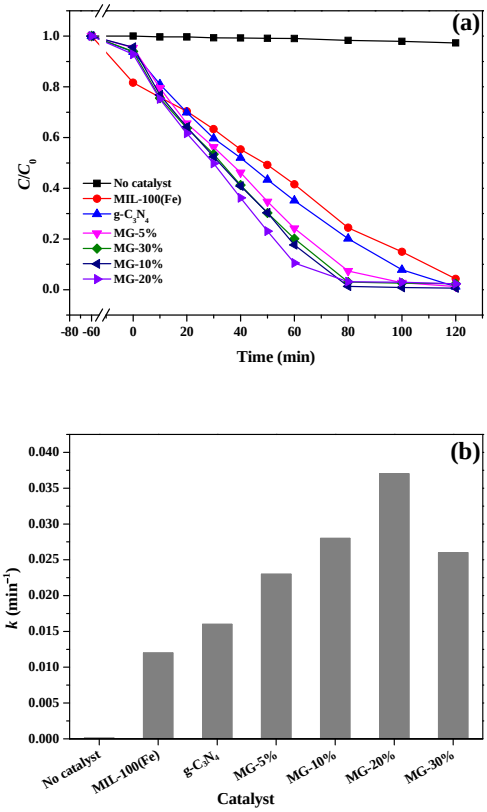

Fig. 8. (a) Cr(VI) reduction photocatalytic performance of MIL-100(Fe), g-C_3N_4, and MG-*x* (*x* = 5%, 10%, 20%, and 30%) hybrids; (b) Rate constant *k* of MIL-100(Fe), g-C_3N_4, and MG-*x* hybrids. For comparison, the photocatalytic performance in a reaction without the catalyst is also given.

active sites of MG-20%, leading to a decline in its photocatalytic activity [52].

$$\text{MG-}x + h\nu \rightarrow \text{MG-}x(h^+ + e^-) \quad (3)$$

$$Cr_2O_7^{2-} + 14H^+ + 6e^- \rightarrow 2Cr^{3+} + 7H_2O \quad (4)$$

$$\text{Organic compounds} + h^+ \rightarrow CO_2 + H_2O + \text{others} \quad (5)$$

$$CrO_4^{2-} + 4H_2O + 3e^- \rightarrow Cr(OH)_3 + 5OH^- \quad (6)$$

The consumption of holes (h^+) will accelerate photoinduced

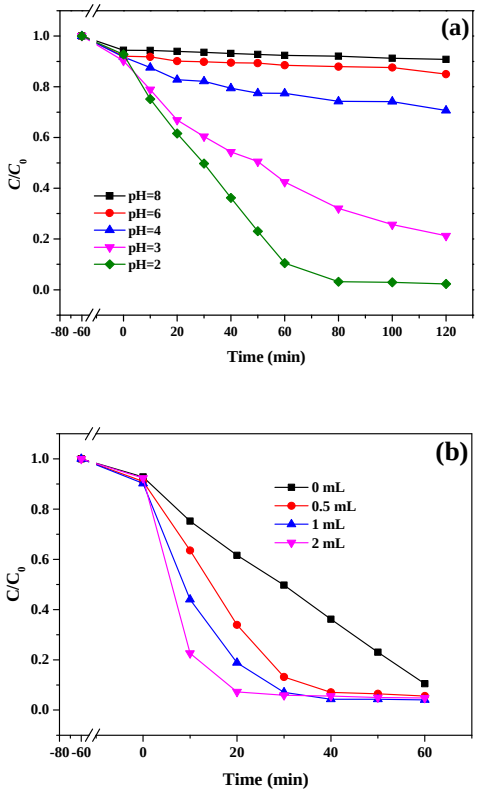

Fig. 9. Photocatalytic activities of the MG-20% hybrid for the reduction of Cr(VI) in aqueous solution at (a) different pH values and (b) different ethanol concentrations.

electron-hole charge separation and result in achieve outstanding Cr(VI) reduction efficiency. To investigate the effect of some organic compounds as hole scavengers on the reduction efficiency, a series of experiments were carried out with the addition of different organic compounds like citric acid, oxalic acid, and diclofenac sodium at pH 2.0. As shown in Fig. 10(a), the addition of hole scavengers (citric acid and oxalic acid) increases the photocatalytic Cr(VI) reduction activity of MG-20%, which might be ascribed to the fact that citric acid and oxalic acid can consume the photoinduced holes produced by the MG-20% photocatalyst upon light irradiation (Eq. (5)) [53]. Thus, more electrons can escape from the pair recombination and become available for the reduction of Cr(VI) under acidic conditions. Ethanol can also capture photoinduced holes, and it was found that an increase in ethanol concentration led to faster Cr(VI) reduction, as shown in Fig. 9(b). However, the addition of diclofenac sodium does not increase the reduction efficiency, as it consumes the hydroxyl radicals, and not photoinduced holes.

To investigate the possible mechanism of the photocatalytic Cr(VI) reduction over MG-20%, the conduction bands (CBs) of MIL-100(Fe) and g-C_3N_4 were determined to be −0.11 and −1.12 V at pH 7.0 (Fig. 11(a) and (b)), respectively, by Mott-Schottky experiments. From the UV-Vis DRS spectra, the band gaps of MIL-100(Fe) and g-C_3N_4 were calculated to be 2.63 and 2.96 eV, respectively. Based on these values, the band structures of MIL-100(Fe) and g-C_3N_4 were determined, and a

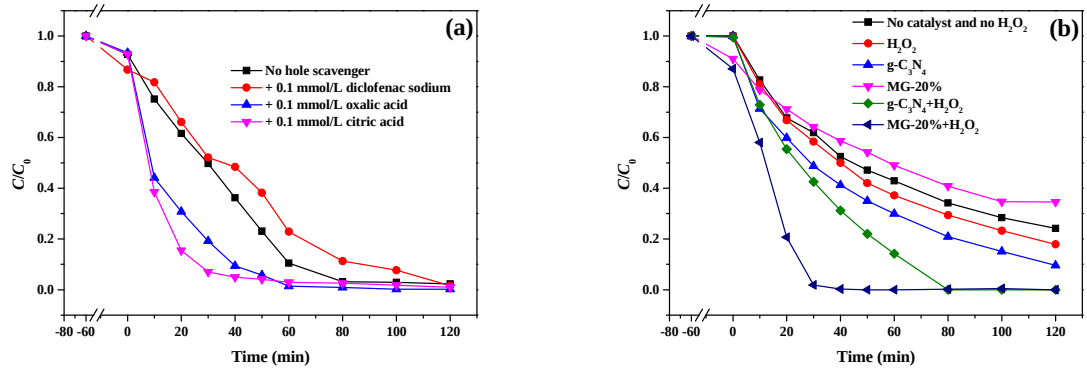

Fig. 10. (a) Photocatalytic activities of the MG-20% hybrid for the reduction of Cr(VI) in the presence of various hole scavengers; (b) Photocatalytic degradation of diclofenac sodium under different control conditions.

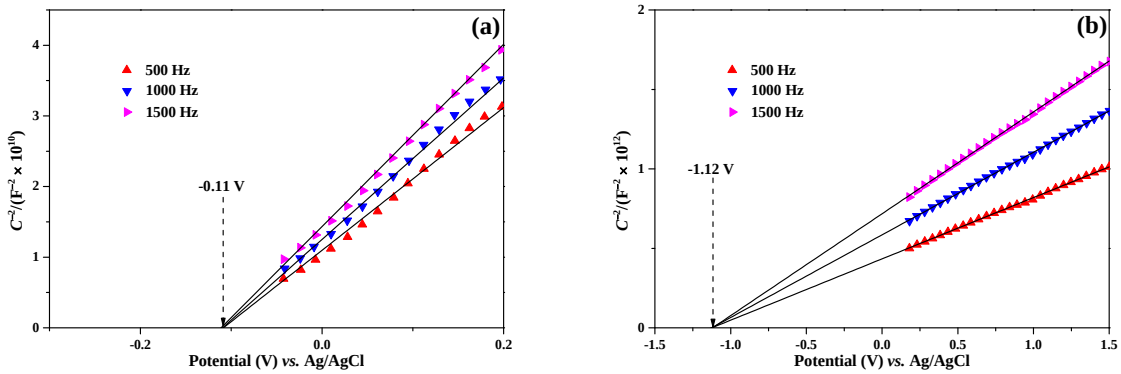

Fig. 11. Mott-Schottky plots of (a) MIL-100(Fe) and (b) g-C_3N_4 in 0.2 mol/L aqueous Na_2SO_4 solution (pH 7.0).

schematic diagram is shown in Fig. 12. Electron-hole pairs can be produced both on MIL-100(Fe) and g-C_3N_4. Fig. 12 illustrates the charge carrier path in the MG-20% system. The photoexcited electrons from the CB of g-C_3N_4 move to the CB of MIL-100(Fe), which can suppress the recombination of photogenerated electron-hole pairs so that more free electrons are gathered in the CB of MIL-100(Fe). Consequently, MG-20% exhibits enhanced photocatalytic activity for Cr(VI) reduction under simulated sunlight irradiation. To further evaluate the photocatalytic performance of the heterojunction structure, the MG-20% was tested for the degradation of diclofenac sodium under different conditions. In the absence of H_2O_2, only 65.4% diclofenac sodium was degraded within 2 h, while 100% degradation was achieved within 50 min after adding H_2O_2, as shown in Fig. 10(b). The above process can be summarized in Eq. (3) and Eqs. (7)–(8) as a Fenton-like reaction occurs [54,55].

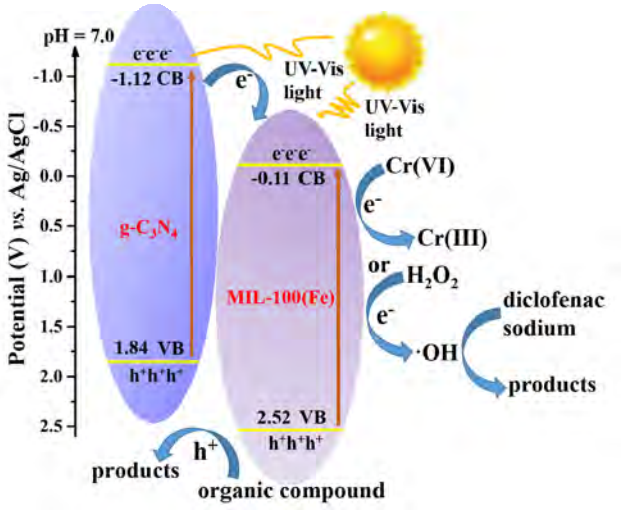

Fig. 12. Possible mechanism of photocatalytic reduction of Cr(VI) and degradation of diclofenac sodium over MG-20%.

$$H_2O_2 + H^+ + e^- \rightarrow H_2O + \cdot OH \quad (7)$$

$$\text{Diclofenac sodium} + \cdot OH \rightarrow \text{Products} \quad (8)$$

To assess the practical application potential of the photocatalysts, the reusability and stability of MG-20% were also investigated. MG-20% was stable after a long-term stability test in an aqueous solution with pH 2.0, for up to 72 h. As shown in Fig. 13(a), the photocatalytic reduction efficiency of MG-20% does not obviously decrease after five runs of Cr(VI) reduction, indicating that the photocatalyst is highly stable and can be used for repeated treatment of Cr(VI). Moreover, the XRD patterns (Fig. 13(b)) of MG-20% before and after the photocatalytic reaction indicated that the crystal structure of MG-20% was not destroyed even after five cycles of the reaction. It can be concluded that MG-20% is stable during the photocatalytic

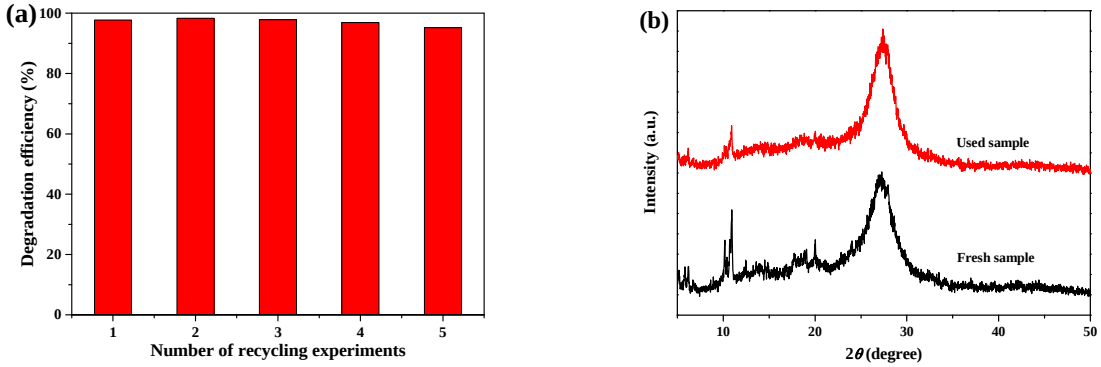

Fig. 13. (a) Reusability of MG-20% in the reduction of Cr(VI); (b) XRD patterns of MG-20% before and after the photocatalytic reaction.

process.

4. Conclusions

The facile fabrication of a series of photocatalytically active MIL-100(Fe)/g-C_3N_4 (MG-*x*) hybrids was accomplished. The optimal MG-20% hybrid demonstrated excellent photocatalytic activity for Cr(VI) reduction and organic pollutant degradation under simulated sunlight irradiation, which was superior to that of pure MIL-100(Fe) and g-C_3N_4. The results of electrochemical measurements and PL emission revealed that the enhanced Cr(VI) reduction was due to the efficient interfacial charge transfer from the photoexcited g-C_3N_4 to MIL-100(Fe). The different hole scavengers and pH value of the reaction solution played important roles in the photocatalytic Cr(VI) reduction. In the photocatalytic system, the addition of ethanol, citric acid, or oxalic acid facilitated the photocatalytic Cr(VI) reduction as the photogenerated holes were easily consumed. Cyclic experiments also indicated the reusability and stability of MG-*x* for the photocatalytic Cr(VI) reduction. This work further demonstrates the great potential application of versatile MOFs and economic g-C_3N_4 for the development of active heterostructured photocatalysts for environmental remediation.

References

[1] R. J. Kieber, J. D. Willey, S. D. Zvalaren, *Environ. Sci. Technol.*, **2002**, 36, 5321–5327.
[2] J. J. Testa, M. A. Grela, M. I. Litter, *Environ. Sci. Technol.*, **2004**, 38, 1589–1594.
[3] S. Loyaux-Lawniczak, P. Lecomte, J. J. Ehrhardt, *Environ. Sci. Technol.*, **2001**, 35, 1350–1357.

Graphical Abstract

Chin. J. Catal., 2019, 40: 70–79 doi: 10.1016/S1872-2067(18)63160-2

Enhanced photocatalytic Cr(VI) reduction and diclofenac sodium degradation under simulated sunlight irradiation over MIL-100(Fe)/g-C_3N_4 heterojunctions

Xuedong Du, Xiaohong Yi, Peng Wang, Jiguang Deng *, Chong-chen Wang *
Beijing University of Civil Engineering and Architecture; Beijing University of Technology

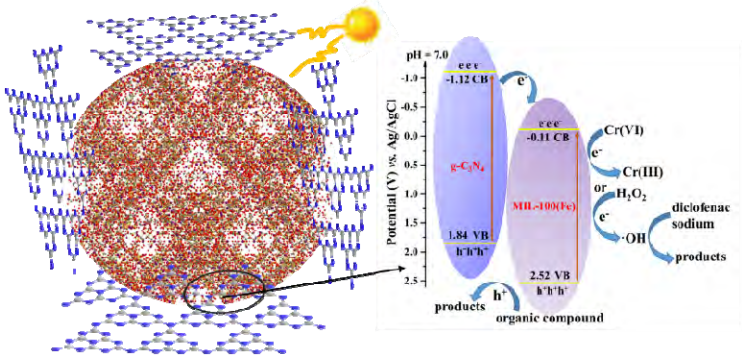

The MIL-100(Fe)/g-C_3N_4 hybrids show high photocatalytic activity under simulated sunlight and can reduce Cr(VI) to Cr(III) and decompose diclofenac sodium effectively.

[4] Y. Li, Y. Bian, H. Qin, Y. Zhang, Z. Bian, *Appl. Catal. B*, **2017**, 206, 293–299.
[5] H. Qin, Y. Bian, Y. Zhang, L. Liu, Z. Bian, *Chin. J. Chem.*, **2017**, 35, 203–208.
[6] M. Zhao, W. Wang, C. Huang, W. Dong, Y. Wang, S. Cheng, H. Wang, H. Qian, *Chin. J. Catal.*, **2018**, 39, 1240–1248.
[7] K. Wei, K. Li, Z. Zeng, Y. Dai, L. Yan, H. Guo, X. Luo, *Chin. J. Catal.*, **2017**, 38, 1804–1811.
[8] C. C. Wang, X. D. Du, J. Li, X. X. Guo, P. Wang, J. Zhang, *Appl. Catal. B*, **2016**, 193, 198–216.
[9] F. X. Wang, X. H. Yi, C. C. Wang, J. G. Deng, *Chin. J. Catal.*, **2017**, 38, 2141–2149.
[10] X. H. Yi, F. X. Wang, X. D. Du, H. Fu, C. C. Wang, *Polyhedron*, **2018**, 152, 216–224.
[11] Y. Zhang, M. Xu, H. Li, H. Ge, Z. Bian, *Appl. Catal. B*, **2018**, 226, 213–219.
[12] D. Guo, R. Wen, M. Liu, H. Guo, J. Chen, W. Weng, *Appl. Organomet. Chem.*, **2015**, 29, 690–697.
[13] W. J. Ong, L. L. Tan, Y. H. Ng, S. T. Yong, S. P. Chai, *Chem. Rev.*, **2016**, 116, 7159–7329.
[14] A. Naseri, M. Samadi, A. Pourjavadi, A. Z. Moshfegh, S. Ramakrishna, *J. Mater. Chem. A*, **2017**, 5, 23406–23433.
[15] H. Lan, L. Li, X. An, F. Liu, C. Chen, H. Liu, J. Qu, *Appl. Catal. B*, **2017**, 204, 49–57.
[16] Y. Wang, X. Zhao, Y. Tian, Y. Wang, A. K. Jan, Y. Chen, *Chem. Eur. J.*, **2017**, 23, 419–426.
[17] L. Gu, J. Wang, Z. Zou, X. Han, *J. Hazard. Mater.*, **2014**, 268, 216–223.
[18] J. Zhang, M. Zhang, R. Q. Sun, X. Wang, *Angew. Chem. Int. Ed.*, **2012**, 51, 10145–10149.
[19] Y. Cui, Y. Wang, H. Wang, F. Cao, F. Chen, *Chin. J. Catal.*, **2016**, 37, 1899–1906.
[20] L. Ge, C. Han, J. Liu, *Appl. Catal. B*, **2011**, 108–109, 100–107.
[21] S. Zhao, X. Zhao, S. Ouyang, Y. Zhu, *Catal. Sci. Technol.*, **2018**, 8, 1686–1695.
[22] S. Zhan, F. Zhou, N. Huang, Y. Yin, M. Wang, Y. Yang, Y. Liu, *J. Mol. Catal. A*, **2015**, 401, 41–47.
[23] L. Huang, H. Xu, Y. Li, H. Li, X. Cheng, J. Xia, Y. Xu, G. Cai, *Dalton. Trans.*, **2013**, 42, 8606–8616.
[24] F. Qi, B. Yang, Y. Wang, R. Mao, X. Zhao, *ACS Sustain. Chem. Eng.*, **2017**, 5, 5001–5007.
[25] F. He, G. Chen, Y. Yu, S. Hao, Y. Zhou, Y. Zheng, *ACS. Appl. Mater. Interfaces.*, **2014**, 6, 7171–7179.
[26] C. C. Wang, Y. Q. Zhang, J. Li, P. Wang, *J. Mol. Struct.*, **2015**, 1083, 127–136.
[27] H. Li, S. Yao, H. L. Wu, J. Y. Qu, Z. M. Zhang, T. B. Lu, W. Lin, E. B. Wang, *Appl. Catal. B*, **2018**, 224, 46–52.
[28] C. C. Wang, J. R. Li, X. L. Lv, Y. Q. Zhang, G. S. Guo, *Energy Environ. Sci.*, **2014**, 7, 2831–2867.
[29] J. Qiu, X. Zhang, Y. Feng, X. Zhang, H. Wang, J. Yao, *Appl. Catal. B*, **2018**, 231, 317–342.
[30] L. Shen, R. Liang, L. Wu, *Chin. J. Catal.*, **2015**, 36, 2071–2088.
[31] S. Wang, J. Lin, X. Wang, *Phys. Chem. Chem. Phys.*, **2014**, 16, 14656–14660.
[32] R. Wang, L. Gu, J. Zhou, X. Liu, F. Teng, C. Li, Y. Shen, Y. Yuan, *Adv. Mater. Interfaces*, **2015**, 2, 1500037/1–1500037/5.
[33] H. Wang, X. Yuan, Y. Wu, G. Zeng, X. Chen, L. Leng, H. Li, *Appl. Catal. B*, **2015**, 174–175, 445–454.
[34] J. Hong, C. Chen, F. E. Bedoya, G. H. Kelsall, D. Ohare, C. Petit, *Catal. Sci. Technol.*, **2016**, 6, 5042–5051.
[35] S. Panneri, M. Thomas, P. Ganguly, B. N. Nair, A. P. Mohamed, K. G. K. Warrier, U. S. Hareesh, *Catal. Sci. Technol.*, **2017**, 7, 2118–2128.
[36] Y. Gong, X. Zhao, H. Zhang, B. Yang, K. Xiao, T. Guo, J. Zhang, H. Shao, Y. Wang, G. Yu, *Appl. Catal. B*, **2018**, 233, 35–45.
[37] W. Huang, N. Liu, X. Zhang, M. Wu, L. Tang, *Appl. Surf. Sci.*, **2017**, 425, 107–116.
[38] P. Horcajada, S. Surblé, C. Serre, D. Y. Hong, Y. K. Seo, J. S. Chang, J. M. Grenèche, I. Margiolaki, G. Férey, *Chem. Commun.*, **2007**, 2820–2822.
[39] Y. C. Zhang, J. Li, M. Zhang, D. D. Dionysiou, *Environ. Sci. Technol.*, **2011**, 45, 9324–9331.
[40] S. H. Huo, X. P. Yan, *J. Mater. Chem.*, **2012**, 22, 7449–7455.
[41] S. Hu, L. Ma, J. You, F. Li, Z. Fan, F. Wang, D. Liu, J. Gui, *RSC Adv.*, **2014**, 4, 21657–21663.
[42] Q. Huang, J. Yu, S. Cao, C. Cui, B. Cheng, *Appl. Surf. Sci.*, **2015**, 358, 350–355.
[43] X. Huang, C. Tan, Z. Yin, H. Zhang, *Adv. Mater.*, **2014**, 26, 2185–2204.
[44] F. Dong, L. Wu, Y. Sun, M. Fu, Z. Wu, S. C. Lee, *J. Mater. Chem.*, **2011**, 21, 15171–15174.
[45] Y. Gao, S. Li, Y. Li, L. Yao, H. Zhang, *Appl. Catal. B*, **2017**, 202, 165–174.
[46] F. Zhang, J. Shi, Y. Jin, Y. Fu, Y. Zhong, W. Zhu, *Chem. Eng. J.*, **2015**, 259, 183–190.
[47] J. Qu, D. Chen, N. Li, Q. Xu, H. Li, J. He, J. Lu, *Appl. Catal. B*, **2017**, 207, 404–411.
[48] Z. Tong, D. Yang, T. Xiao, Y. Tian, Z. Jiang, *Chem. Eng. J.*, **2015**, 260, 117–125.
[49] Y. Zang, L. Li, X. Li, R. Lin, G. Li, *Chem. Eng. J.*, **2014**, 246, 277–286.
[50] F. Tan, M. Liu, K. Li, Y. Wang, J. Wang, X. Guo, G. Zhang, C. Song, *Chem. Eng. J.*, **2015**, 281, 360–367.
[51] Q. Yang, Q. Zhao, S. S. Ren, Q. Lu, X. Guo, Z. Chen, *J. Solid State Chem.*, **2016**, 244, 25–30.
[52] F. Zhang, Y. Zhang, G. Zhang, Z. Yang, D. D. Dionysiou, A. Zhu, *Appl. Catal. B*, **2018**, 236, 53–63.
[53] L. Yang, Y. Xiao, S. Liu, Y. Li, Q. Cai, *Appl. Catal. B*, **2010**, 94, 142–149.
[54] M. Cheng, C. Lai, Y. Liu, G. Zeng, D. Huang, C. Zhang, L. Qin, L. Hu, C. Zhou, W. Xiong, *Coordin. Chem. Rev.*, **2018**, 368, 80–92.
[55] D. Wang, M. Wang, Z. Li, *ACS Catal.*, **2015**, 5, 6852–6857.

模拟太阳光照射下MIL-100(Fe)/g-C_3N_4异质结光催化Cr(VI)还原和双氯芬酸钠降解

杜雪冬[a]，衣晓虹[a]，王　鹏[a]，邓积光[b,*]，王崇臣[a,#]
[a]北京建筑大学建筑结构与环境修复功能材料北京市重点实验室，北京100044
[b]北京工业大学环境与能源工程学院化学与化工系，北京100022

摘要: 有毒重金属离子Cr(VI)广泛应用于制革、电镀、印刷、颜料和抛光等行业, 因而成为地表水和地下水中常见的污染

物. 光催化还原Cr(VI)为**Cr(III)**利用可持续能源太阳能, 费用低且没有二次污染问题已经受到广泛关注. g-C_3N_4是一种稳定性好且能吸收可见光的优异光催化材料, 但也具有比表面积小及电子和空穴容易复合等缺点. 为进一步提高g-C_3N_4的光催化效率, 人们合成了各种新型复合材料, 如g-C_3N_4/Bi_2WO_6, g-C_3N_4/SiW_{11}和g-C_3N_4/$Zn_3V_2O_7(OH)_2(H_2O)_2$等.

本文通过非常简便的球磨-煅烧法制备了金属-有机骨架材料MIL-100(Fe)与类石墨结构氮化碳（g-C_3N_4）的异质结结构(MG-*x*, *x* = 5%, 10%, 20%和30%, 代表MIL-100(Fe)占复合物的质量分数), 并对复合材料进行了粉末X射线衍射(PXRD)、红外光谱(FTIR)、热重(TGA)、透射电镜(TEM)、紫外-可见漫反射光谱(UV-Vis DR)和荧光光谱(PL)等表征. 实验研究了MG-*x*在模拟太阳光照射下光催化还原Cr(VI)和降解双氯芬酸钠的性能, 考察了空穴捕捉剂(乙醇、柠檬酸、草酸和双氯芬酸钠)和pH值(2–8)对光催化还原Cr(VI)效率的影响.

实验结果表明, PXRD谱图显示复合物的衍射峰位置均与MIL-100(Fe)及g-C_3N_4的峰位置相吻合, 球磨和煅烧后无新衍射峰产生. TEM图片证明复合物中g-C_3N_4附着在MIL-100(Fe)表面. 光照80 min后, MG-*x*复合物的还原效率均大于92%, 高于MIL-100(Fe)(75.6%)和g-C_3N_4(79.8%)的还原效率. 其中, MG-20%的光催化活性最高, 还原效率达到97.0%, 且还原Cr(VI)的速率分别是MIL-100(Fe)的3.08倍和g-C_3N_4的2.31倍. 随着MIL-100(Fe)含量的增加, 复合物的光催化活性先增后减. 这是因为MIL-100(Fe)含量的增加不仅有利于电荷的转移, 也有利于可见光的利用, 然而过多的MIL-100(Fe)可能会影响异质结的质量, 不利于电荷的转移. 随着溶液pH值的从2提高到8, 还原效率从98%降低到9%. 这是因为在酸性条件下H^+浓度高有利于Cr(VI)还原为Cr(III), 而当pH>6时, Cr^{3+}与OH^-形成$Cr(OH)_3$沉淀附着在催化剂表面, 影响对光的吸收, 降低了光催化效率. 当反应体系中加入乙醇、柠檬酸和草酸时, 光催化速率提高, 而加入双氯芬酸钠后光催化速率未见提高, 这是由于小分子链烃有机物容易捕捉光生空穴, 而双氯芬酸钠不能有效捕捉MG-20%产生的光生空穴. 电化学测试证明g-C_3N_4的光生电子可转移到MIL-100(Fe)的导带, 复合物提高了光生电子和光生空穴的分离效率, 从而提高了光催化还原Cr(VI)的活性. 同时, 在加入H_2O_2的条件下, MG-20%在50 min内光催化降解双氯芬酸钠的效率达到100%. MG-20%循环使用5次后, 光催化效率没有明显降低, 光催化剂的XRD谱没有发生明显变化, 证明其具有很好的稳定性. 综上, 本研究提供了一种具有应用前景的高效MOF/g-C_3N_4复合物光催化剂.

关键词: MIL-100(Fe); g-C_3N_4; 异质结; 六价铬还原; 双氯芬酸钠

收稿日期: 2018-07-24. 接受日期: 2018-09-12. 出版日期: 2019-01-05.

*通讯联系人. 电话/传真: (010)67391767; 电子信箱: jgdeng@bjut.edu.cn

#通讯联系人. 电话/传真: (010)61209186; 电子信箱: wangchongchen@bucea.edu.cn

基金来源: 国家自然科学基金(51578034, 51878023); 北京市属高校高水平教师队伍建设支持计划长城学者培养计划(CIT&TCD20180323); 北京市属高校高层次人才引进与培养计划和创新团队与教师职业发展计划(IDHT20170508); 北京百千万人才项目(2017A38); 北京市属高校基本科研业务费专项资金(X18075/X18076/X18124/X18125/X18276); 北京建筑大学校设基金(KYJJ2017033/KYJJ2017008).

本文的电子版全文由Elsevier出版社在ScienceDirect上出版(http://www.sciencedirect.com/science/journal/18722067).